Arabian Journal of Chemistry (2020) 13, 2858–2864

King Saud University

Arabian Journal of Chemistry

www.ksu.edu.sa
www.sciencedirect.com

ORIGINAL ARTICLE

Preparation of nanoparticulate TiO_2 containing nanocrystalline phases of anatase and brookite by electrochemical dissolution of remelted titanium components

D. Ortega-Díaz [a,b,1], D. Fernández [a,b], S. Sepúlveda [c], R.R. Lindeke [d], J.J. Pérez-Bueno [a], E. Peláez-Abellán [b,1], J. Manríquez [a,*,1]

[a] *Centro de Investigación y Desarrollo Tecnológico en Electroquímica S.C., Parque Tecnológico Querétaro s/n, Sanfandila, 76703 Pedro Escobedo, Querétaro, Mexico*
[b] *Facultad de Química, Universidad de la Habana, Calzada de Zapata s/n esq. Calle G, 10400 El Vedado, La Habana, Cuba*
[c] *Centro de Innovación, Investigación y Desarrollo en Ingeniería y Tecnología, Universidad Autónoma de Nuevo León, Nuevo León, Mexico*
[d] *MIE@UMD United States of America and Peace Corps Volunteer Mexico, Mexico*

Received 24 April 2018; accepted 21 July 2018
Available online 29 July 2018

KEYWORDS

Remelted titanium components;
Re-use;
Nano-crystalline TiO_2 electro-synthesis;
High faradaic efficiency

Abstract In this investigation, we present an efficient electrochemical methodology to prepare nano-particulate TiO_2 having a nano-crystalline composition of 40% Anatase and 60% Brookite, without need for subsequent thermal treatments (which are typically applied to alter the amount of amorphicity). This procedure for oxide synthesis is novel as it involves the galvanostatic dissolution of remelted Titanium Components, thus constituting a promising technological route for re-using Titanium-containing metallic pieces from the secondary metals industry to produce nano-crystalline TiO_2 powders as a high value-added primary product. The experimental results presented showed that the faradaic efficiency of the TiO_2 electro-synthesis, crystalline purity, and dispersion of the electro-generated TiO_2 material was significant, despite the fact that the titanium content of the remelted titanium components was less than 80%.

* Corresponding author.
E-mail address: jmanriquez@cideteq.mx (J. Manríquez).
[1] These authors contributed equally to this work.
Peer review under responsibility of King Saud University.

Production and hosting by Elsevier

1. Introduction

Titanium dioxide (TiO_2) has been widely investigated due to its opto-electronic properties, photo- and chemical stability and very low toxicity. Crystalline TiO_2 is usually prepared in three phases: Anatase, Rutile, and Brookite. Rutile is the most thermodynamically stable phase, but Anatase and Brookite are

https://doi.org/10.1016/j.arabjc.2018.07.015
1878-5352 © 2018 Production and hosting by Elsevier B.V. on behalf of King Saud University.
This is an open access article under the CC BY-NC-ND license (http://creativecommons.org/licenses/by-nc-nd/4.0/).

more photo-active. Furthermore, the reduction of the particle size of this semiconductor material increases the specific surface area, thus improving its ability to harvest light because of increased numbers of charge carriers. Among other applications, employment of photo-electrochemical behavior of TiO_2 for preparing efficient photo-catalysts (Kim et al., 2016; Ansari and Cho, 2016; Ren et al., 2015), dye-sensitized solar cells (Ghadiri et al., 2016; Chava et al., 2016; Chang et al., 2016; Hossain et al., 2015), biosensors (Viter et al., 2012; Viter et al., 2017; Wang et al., 2017), and biomedical devices (Kulkarni et al., 2015; Castagnola et al., 2017) is important.

Several methodologies have been used to prepare nano-particulate TiO_2 from titanium-based precursors. One well-known method is the hydrothermal process, which is usually carried out in pressurized stainless steel autoclaves at well-controlled temperature and pressure conditions. Although the crystallinity of the materials obtained is often acceptable, it requires extended preparation time (de Mendonça et al., 2017; Yao et al., 2017; Zhou et al., 2017). On the other hand, the sol–gel method is the most often employed synthesis process. It involves the formation of a colloidal suspension from the hydrolysis and subsequent polymerization reactions of the precursors such as titanium alkoxides (Priyanka et al., 2014; Lu et al., 2017; Hinojosa-Reyes et al., 2017). However, the reactions involved by this method are very fast, thus it is difficult to control nanoparticle size and dispersion in polar solvents. Therefore, this process typically produces amorphous particles requiring thermal treatments after the synthesis to improve crystallinity. During the thermal treatments phase transformations could have adverse effects on the stability of the TiO_2 nanostructure (Guohui et al., 2012; Cihlar et al., 2015). Contrarily, electrochemical processes have been successfully utilized to prepare TiO_2 nano-structures, such as nano-grass and nano-tubes (Bezares et al., 2015), starting from high purity titanium foils anodized in aqueous solutions containing oxygen donors (e.g. H_3PO_4 and glycols). However, the capability of these methods to generate TiO_2 nanoparticles have been only minimally studied.

In this work, we present an efficient, electrochemical methodology to prepare nano-particulate TiO_2, containing anatase and brookite nano-crystalline phases, without need for subsequent thermal treatments to reduce amorphicity. This procedure is novel because it utilizes the galvanostatic dissolution of remelted titanium components from the secondary metals industry. Interestingly, the results presented showed that the faradaic efficiency of the TiO_2 electro-synthesis, crystalline purity, and dispersion in aqueous medium of the electro-generated TiO_2 material were significant, despite the fact that the typical Ti content of the remelted titanium components was less than 80%.

2. Experimental section

2.1. Electrochemical preparation of nanoparticulate TiO_2

Nanoparticulate TiO_2 was galvanostatically prepared in a 2-electrode cell having an 800 cm^2 cylindrical tube of SAE-AISI 1018 steel (cathode). The anode was an 80 cm^2 square plate, hand-cutted from a sample of remelted titanium component (see elemental composition in Table 1) positioned in the center of the cylindrical cathode. Prior to use, the Ti-containing anode was immersed in concentrated HF (J.T. Baker, 49.9 wt%) for 10 s and then washed with copious amounts of deionized water (having a resistivity of 18.18 MΩ cm). The electrolysis cell was filled with 350 mL of an aqueous solution containing 50 v/v% ethanol (J.T. Baker, 94.7%), plus 0.13 M NaCl (Fermont, 99.6%) and 0.01 M sodium dodecyl sulfate (SDS, Sigma-Aldrich, 99%). The ionic conductance of this electrolytic solution was 10 μS cm^{-1} at 25 °C.

A current density of 4 mA cm^{-2}, with continual stirring, was passed through the anode to produce nano-particulate TiO_2. Electro-generation of TiO_2 was experimentally observed as the Ti-containing anode dissolved according to Reaction (1) (Bratsch, 18 (1989)). The reaction began immediately upon current onset. After 1 h of anodic dissolution, the current was turned off and the white TiO_2 nano-particles were filtered from the electrolyte. The filtrate product was washed and dried at room temperature prior to characterization.

$$Ti + 2H_2O \rightarrow TiO_2 + 4H^+ + 4e^- \quad (1)$$

2.2. Characterization of electro-generated TiO_2

2.2.1. Particle size distribution and ζ-potential measurements

TiO_2 particle size distribution and ζ-potential were measured in an aqueous 2 mg L^{-1} TiO_2 colloidal suspension at 25 °C by utilizing a Malvern Zetasize ZS particle analyzer, operated using a Dynamic Light Scattering (DLS) approximation. The dispersion angle was scanned from 15° to 90°. The analyzed TiO_2 suspension was sonicated for 15 min at 42 kHz prior to testing.

2.2.2. Specific surface area measurements

BET surface area of the electro-generated TiO_2 samples was measured in 200.13 ± 1.27 m^2 g^{-1} in a Micromeritics TriStar II surface area analyzer. The analyzer was operated accordingly to the adsorptive analysis of N_2 (cross-sectional area = 0.1620 m^2 $molecule^{-1}$) procedure. We report these findings in the Supplementary Data Section.

Supplementary data associated with this article can be found, in the online version, at https://doi.org/10.1016/j.arabjc.2018.07.015.

2.2.3. X-Ray diffraction (XRD) and Raman spectroscopy analysis

XRD analysis of the TiO_2 nanoparticles was performed using a Bruker D8 Advance diffractometer equipped with a CuKα1 source (λ = 1.5405 Å). The 2 θ diffraction angle was scanned from 10° to 80° (resolution 0.078° min^{-1}). Rietveld analysis was carried out using the software: MAUD version 2.55. Additionally, Raman spectroscopy of the TiO_2 materials was performed using a Horiba-Jobin-Yvon LabRAM spectrometer, equipped with a 14 mW 780 nm laser.

2.2.4. Electron microscopy studies

High-Resolution Scanning Electron Microscopy (HR-SEM) images and Energy-Dispersive X-ray Spectroscopy (EDS) analysis of TiO_2 nanoparticles was conducted using a FEI Nova NanoSEM 200 microscope operated in field emission

Table 1 Elemental composition of the remelted titanium component which were employed in this work to prepare nano-particulate TiO_2 material.

Element	Si	Fe	Cr	Ni	Ti
wt. %	4.50 ± 0.10	5.17 ± 0.05	5.93 ± 0.05	6.63 ± 0.05	77.73 ± 0.15

modality and an accelerating voltage of 20 kV. Further Transmission Electron Microscopy (TEM) images and Selected Area Electron Diffraction (SAED) patterns of cross-sectional TiO_2 nanoparticles were developed with a FEI Titan G2 80–300 microscope at an accelerating voltage of 120 kV. The nano-particulate TiO_2 samples were placed on the surface of a 400 mesh (3.05 mm O.D.) carbon-coated copper Gilder grid before placement in the microscope.

2.2.5. X-ray photoelectron spectroscopy (XPS) analysis

XPS analysis was conducted using a Thermo Fisher Scientific K-Alpha spectrometer, equipped with an Al Kα source (λ = 1487 eV). The analysis chamber was maintained at an ultra-high vacuum pressure (UHVP) of 1×10^{-9} mbar, while the survey and high-resolution core level spectra were collected employing a 2000 μm spot size and a pass energy of 23.5 eV. In all the cases, the O_{1s} peak signal at 530.0 eV provided an internal standard by experimental convenience. After completing the analyses, a Shirley-type background subtraction was performed prior to fitting mixed Gaussian-Lorentzian functions to the experimental spectra.

3. Results and discussion

3.1. Faradaic efficiency of nanoparticulate TiO_2 electrogeneration

Faradic efficiency (ξ) was estimated at 84% using Relationship 2. Here, j (set at 4 mA cm^{-2}) is the total current passed through the cell during a time t (in sec), A_g (80 cm^2) is geometric area of the Ti-containing anode, n (equal to 4) is the number of electrons involved in Reaction (1), and F is Faraday's constant (96500 C mol^{-1}). Additionally, m_{TiO_2} (0.20 g) and M_{TiO_2} (79.86 g mol^{-1}) are the mass and molecular weight of the electro-generated TiO_2, respectively (Pletcher, 1991). This important result clearly indicates that the electrochemical preparation of nano-particulate TiO_2 was very efficient.

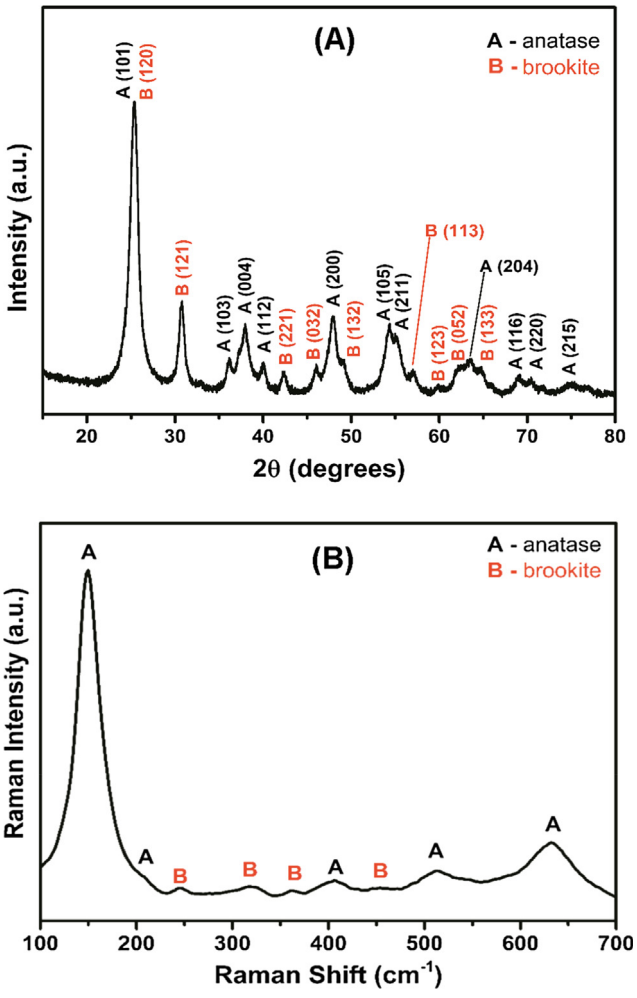

Fig. 2 (A) X-ray diffractogram and (B) Raman spectrum obtained from a sample of electro-generated TiO_2 material.

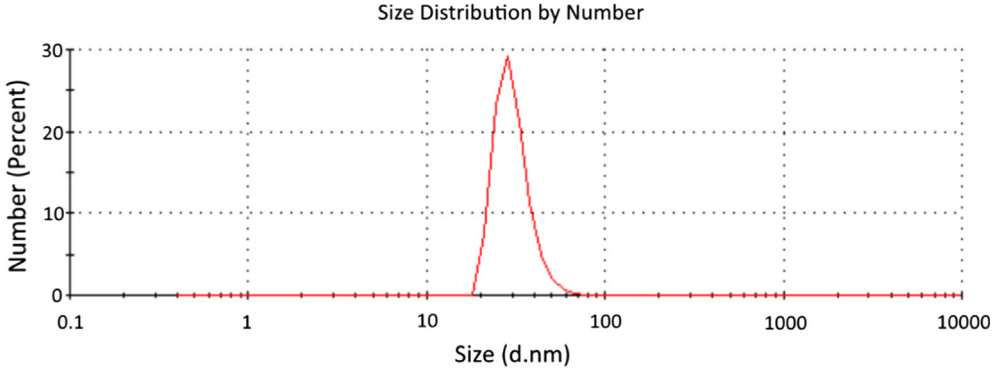

Fig. 1 Particle size distribution measurements obtained for an aqueous suspension of electro-generated TiO_2 material.

$$\xi = \frac{charge\ \ consumed\ \ in\ \ Reaction\ \ 1}{total\ \ charge\ \ passed} \times 100\% = \frac{\left(\frac{m_{TiO_2}}{M_{TiO_2}}\right) \cdot n \cdot F}{j \cdot A_g \cdot t} \times 100\% \quad (2)$$

3.2. Particle size distribution and ζ-potential measurements

Fig. 1 shows the particle size distribution obtained from an aqueous suspension of electro-generated TiO_2, which clearly reveals a colloidal system constituted by TiO_2 nano-particles having an average size of 29 nm. Complementarily, ζ-potential was measured in −62 mV at the same TiO_2 colloidal suspension, an indicating of very good suspension stability (Salopek et al., 1992).

3.3. X-Ray diffraction (XRD) and Raman spectroscopy analysis

Crystalline phases were identified in the electro-generated TiO_2 by XRD Fig. 2A) and Raman spectroscopy Fig. 2B) analyses. During XRD analysis, the interplanar spacing was calculated using JCPDS files 21-1272 (anatase) and 29-1360 (brookite). A detailed review of Fig. 2A reveals a set of 8 characteristic signals for 2θ at 38°, 47°, 53°, 55°, 67°, 68°, 70° and 75°, which seem to be the anatase planes A(1 0 1), A(0 0 4), A(2 0 0), A (1 0 5), A(2 1 1), A(2 0 4), A(1 1 6), A(2 2 0), and A(2 1 5), respectively. Furthermore, the same review indicate another set of 8 characteristic signals localized at 2θ of 31°, 42°, 45°, 49°, 57°, 60°, 62°, and 66°, which should correspond to brookite planes B(1 2 1), B(2 2 1), B(0 3 2), B(1 3 2), B(1 1 3), B(1 2 3), B(0 5 2), and B(1 3 3), respectively. Additionally, an intense

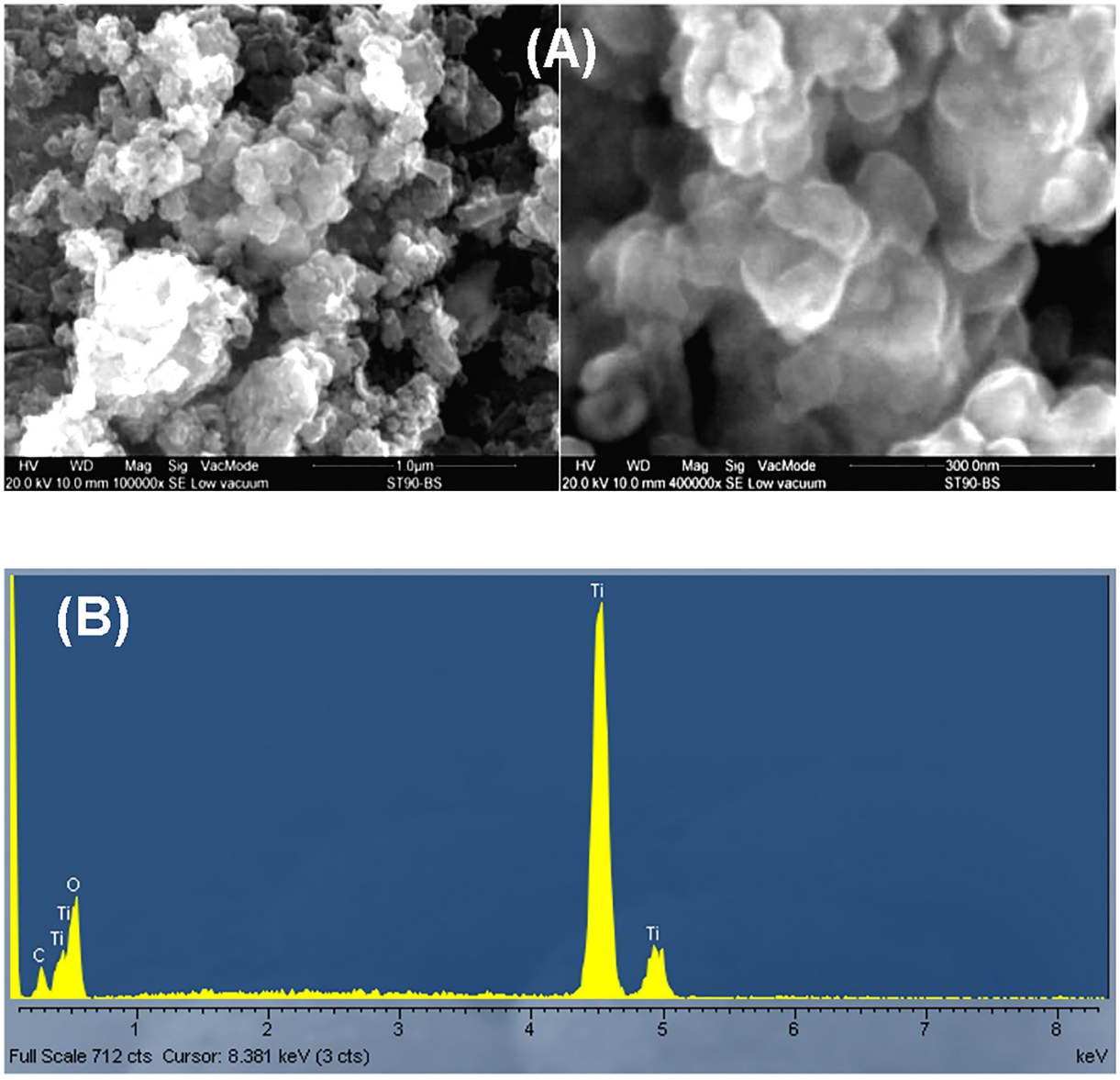

Fig. 3 (A) SEM images and (B) EDS analysis obtained from a sample of electro-generated TiO_2 material. SEM images are presented at magnifications of 100 and 400 kX (for comparative purposes).

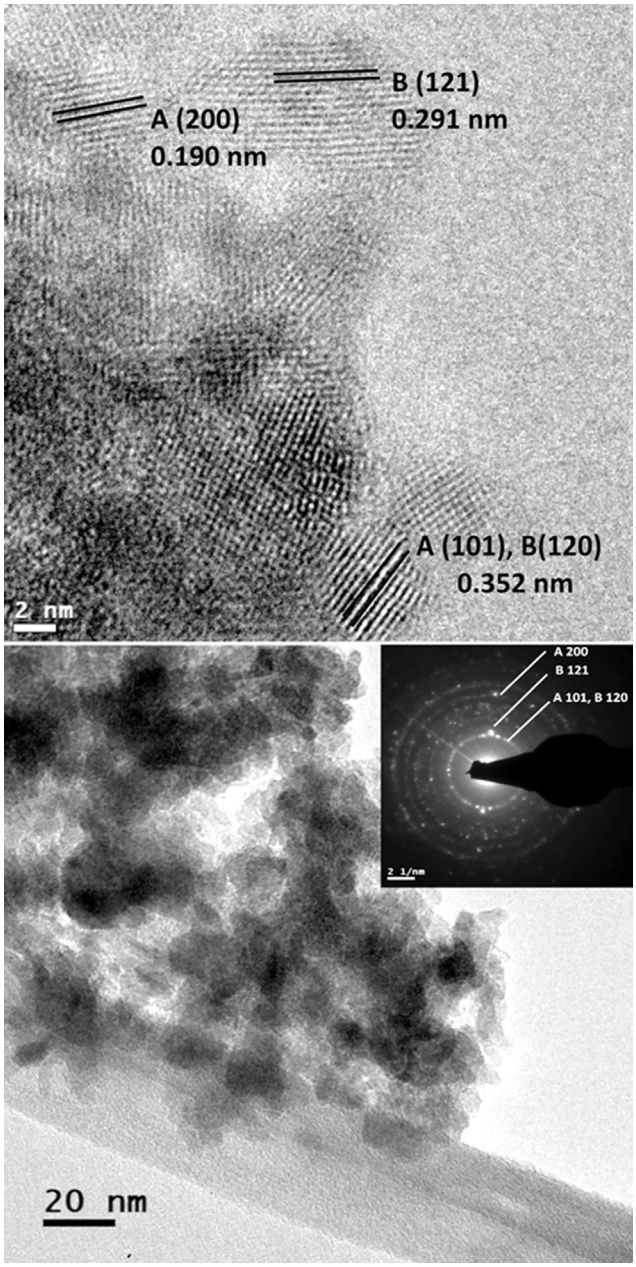

Fig. 4 TEM images and SAED patterns (inset) of cross-sections of electro-generated TiO_2 particles. The interplanar distances of the anatase and brookite crystalline phases were identified.

signal was localized at $2\theta = 25°$ in Fig. 2A, which can be associated with the overlapping of the diffraction of planes A(1 0 1) and B(1 2 0), for anatase and brookite, respectively.

Reviewing Fig. 2B confirmed the presence of a set of anatase characteristic bands at 406, 512 and 634 cm^{-1}, corresponding to the vibrational modes B_{1g}, A_{1g}, and E_g (Kaplan et al., 2016; Leyva-Porras et al., 2015). It also confirmed the presence of a set of brookite characteristic bands at 246, 318, 362 and 452 cm^{-1}, corresponding to brookite's vibrational modes A_{1g}, B_{3g}, B_{2g}, and B_{2g} (Cao et al., 2016; Shen et al., 2013; Tran et al., 2017). Additionally, one observes the very intense band localized at 150 cm^{-1}, corresponding to the overlap of the vibrational modes E_g and A_{1g} of anatase and brookite phases, respectively. This observation supports the results obtained from the XRD analysis and strongly suggests the existence of anatase|brookite junctions within the lattice of the electro-generated TiO_2 nano-particles (El-Sheikh et al., 2017).

3.4. Electron microscopy studies

Fig. 3 shows HR-SEM Fig. 3A) and EDS studies Fig. 3B) of a sample of the electro-generated TiO_2 nano-particles. On first viewing of Fig. 3A one observes sub-100 nm TiO_2 agglomerates, whereas a detailed examination of Fig. 3B revealed an elemental composition consisting of Ti and O (as the main inorganic elements) and C (as an organic impurity). It was reasonable to expect detection of the presence of C-based impurities since SDS was employed as a tenso-active additive in the electro-synthesis electrolytic solution.

A comparison between TEM images Fig. 4A) and SAED pattern Fig. 4B-*inset*) of cross-sections of TiO_2 particles confirmed the nano-crystalline structure of the electro-generated TiO_2 powders, supporting the results of the particle size distribution reported in Section 3.2. A detailed exploration of Fig. 4A and Table 2 reveal the presence of TiO_2 nanostructures that conformed to 7 nm (anatase) and 13 nm (brookite) crystallites, distributed in a crystalline fraction of 40% anatase and 60% brookite. These results are well supported by the BET surface areas reported for the electro-generated TiO_2 (200.13 ± 1.27 $m^2\ g^{-1}$) in Section 2.2.2, and for the commercial Degussa® P25 TiO_2 (56 $m^2\ g^{-1}$, nominal crystallites size of 21 nm (Raj and Viswanathan, 2009). Moreover, a comparison between Fig. 4A and B revealed the presence of the characteristic A(2 0 0) and B(1 2 1) planes, but also confirmed the existence of nano-metric anatase|brookite junctions in the TiO_2 lattice. This conclusion was supported by the appearance of overlapped A(1 1 0) and B(1 2 0) planes at TEM images and SAED pattern (El-Sheikh et al., 2017).

3.5. X-ray photoelectron spectroscopy (XPS) analysis

Fig. 5 shows the results of the XPS analysis obtained from a sample of the electro-generated TiO_2 material. In particular,

Table 2 Crystalline composition, crystallites average sizes and lattice parameters estimated by Rietveld analysis of the XRD spectrum obtained for a sample of electro-generated TiO_2 material.

Crystalline fraction (%)		Crystallite size (nm)		Lattice parameter (Å)					
Anatase	Brookite	Anatase	Brookite	Anatase			Brookite		
40	60	7.4	12.7	*a*	*b*	*c*	*a*	*b*	*c*
				3.802	3.802	9.462	9.179	5.450	5.163

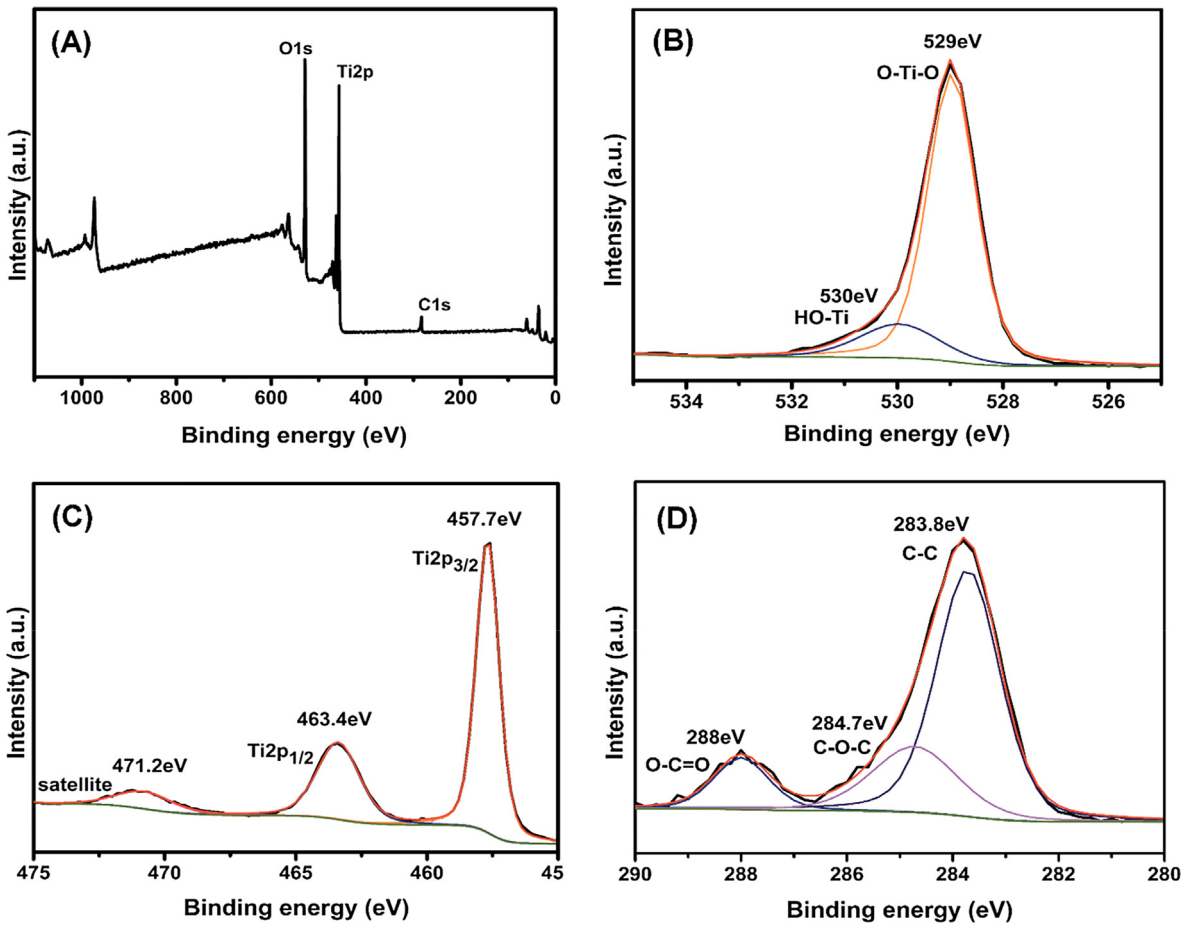

Fig. 5 XPS spectra obtained for electro-generated TiO_2 material where, (A) survey spectrum, (B, C and D) high-resolution core level spectra corresponding to O, Ti, and C, respectively.

Fig. 5A shows the survey XPS spectrum with two signals detected at 457 and 529 eV, which correspond to the emitted electrons' energies from the Ti_{2p} and O_{1s} orbitals, respectively. Additionally, the single signal localized at 278 eV was associated with the emitted electrons' energy from C_{1s} orbitals. These data clearly confirmed the presence of Ti, O, and C as the main elements contained in the TiO_2 lattice.

Fig. 5B and C shows the high-resolution core level XPS spectra for O and Ti. Reviewing Fig. 5B reveals two signals: at 529 and 530 eV, which were associated with the emitted electrons' energies from the O_{1s} orbitals in an O—Ti—O and Ti—OH binding scheme, respectively (Si et al., 2018; Naseema et al., 2018). Additionally, a spin-orbital splitting of the emitted electrons' energies from the Ti_{2p} orbitals can be observed in Fig. 5C at 458 and 463 eV, which correspond to the signals-coupling $Ti^{4+}_{2p_{3/2}}$ and $Ti^{4+}_{2p_{1/2}}$, respectively. Since there was an absence of the $Ti^{3+}_{2p_{1/2}}$ characteristic signal around 460 eV in Fig. 5C, the team concluded that Ti^{4+} is predominant within the TiO_2 lattice (Atuchin et al., 2006; Bharti et al., 2016).

A further comparative exploration of Fig. 5B and D reveals the weak intensities of the signals localized at 530 eV (in Fig. 5B) and 286 eV (in Fig. 5D) suggesting the presence of very few Ti—OH and C—O—C bindings at the TiO_2 lattice. However, a detailed review of Fig. 5C, clearly reveals that the content of O—C═O and C—C bindings in the TiO_2 lattice indicated by significantly strong intensities of their respective signals (288 and 284 eV). Again, this observation could be reasonably expected following the addition of tenso-active SDS into the electro-synthesis electrolytic solution which could leave residuals (Yi et al., 2017). However, we have shown earlier that the presence of C-based impurities do not significantly affect the electrical and photo-catalytic properties of nano-crystalline TiO_2 powders (Manríquez and Godínez, 2007; Peralta-Hernández et al., 2007).

4. Conclusions

Nano-crystalline TiO_2 nano-particles, with acceptable chemical purity, was successfully prepared by electrochemical dissolution of remelted titanium components from the secondary metals industry. This methodology showed a faradaic efficiency higher than 80% and high level of the desired crystallinity without the need for subsequent thermal treatments. After their electro-generation, studies of the nano-crystalline composition of the TiO_2 material revealed a combination of 40% anatase and 60% brookite phases. The nano-particles so prepared could be employed as environmental photo-catalysts. In addition, the investigation reported here offer a promising technological route for re-using remelted titanium

components, and even "swarf" or chips, to obtain nanocrystalline TiO_2 powders as an alternative, high value-added primary product.

Acknowledgements

The authors thank the Mexican Council for Science and Technology (CONACyT) for its financial support of this work (Grant 258789). D.O.D. acknowledges CONACyT for his PhD scholarship (Grant 639209). The authors also thank Dr. Richard R. Lindeke, PhD (Professor Emeritus, MIE@UMD United States of America and Peace Corps Volunteer Mexico) for his editing service in the English language of this paper. The authors thank Coraquetzali Magdaleno-López, MSc. and Maura Valdéz, BSc for their support during the XPS measurements.

References

Ansari, S.A., Cho, M.H., 2016. Sci. Rep. 6, 25405.
Atuchin, V.V., Kesler, V.G., Pervuhina, N.V., Zhang, Z., 2006. J. Electron. Spectrosc. Relat. Phenom. 152, 18.
Bezares, I., del Campo, A., Herrasti, P., Munoz-Bonilla, A., 2015. Phys. Chem. Chem. Phys. 17, 29319.
Bharti, B., Kumar, S., Lee, H.-N., Kumar, R., 2016. Sci. Rep. 6, 32355.
Bratsch, S.G., 1989. J. Phys. Chem. Ref. Data 18, 21.
Cao, Y., Li, X., Bian, Z., Fuhr, A., Zhang, D., Zhu, J., 2016. Appl. Catal. B 180, 551.
Castagnola, V., Cookman, J., de Araújo, J.M., Polo, E., Cai, Q., Silveira, C.P., Krpetić, Ž., Yan, Y., Boselli, L., Dawson, K.A., 2017. Nanoscale Horiz. 2, 187–198.
Chang, W.-C., Tang, B.-H., Lu, Y.-W., Yu, W.-C., Lin, L.-Y., Wu, R.-J., 2016. J. Power Sources 319, 131.
Chava, R.K., Raj, S., Yu, Y.-T., 2016. J. Alloy. Compd. 672, 212.
Cihlar, J., Kasparek, V., Kralova, M., Castkova, K., 2015. Int. J. Hydrogen Energy 40, 2950–2962.
de Mendonça, V.R., Avansi Jr., W., Arenal, R., Ribeiro, C., 2017. J. Colloid Interface Sci. 505, 454.
El-Sheikh, S.M., Khedr, T.M., Zhang, G., Vogiazi, V., Ismail, A.A., O'Shea, K., Dionysiou, D.D., 2017. Chem. Eng. J. 310, 428.
Ghadiri, E., Zakeeruddin, S.M., Hagfeldt, A., Gratzel, M., Moser, J. E., 2016. Sci. Rep. 6, 24465.
Guohui, Y., Chen, X., Chen, X., Tang, J., Chen, S., 2012. Energy Procedia 16, 1206.
Hinojosa-Reyes, M., Camposeco-Solís, R., Zanella, R., Rodríguez-González, V., 2017. Chemosphere 184, 992.
Hossain, M.A., Park, J., Ahn, J.Y., Park, C., Kim, Y., Kim, S.H., Lee, D., 2015. Electrochim. Acta 173, 665.
Kaplan, R., Erjavec, B., Dražić, G., Grdadolnik, J., Pintar, A., 2016. Appl. Catal. B 181, 465.
Kim, Y., Hwang, H.M., Wang, L., Kim, I., Yoon, Y., Lee, H., 2016. Sci. Rep. 6, 25212.
Kulkarni, M., Mazare, A., Gongadze, E., Perutkova, S., Kralj-Iglic, V., Milosev, I., Schmuki, P., Iglic, A., Mozetic, M., 2015. Nanotechnology 26, 062002.
Leyva-Porras, C., Toxqui-Teran, A., Vega-Becerra, O., Miki-Yoshida, M., Rojas-Villalobos, M., García-Guaderrama, M., Aguilar-Martínez, J.A., 2015. J. Alloy. Compd. 647, 627.
Lu, N., Wang, C., Sun, B., Gao, Z., Su, Y., 2017. Sep. Purif. Technol. 186, 226.
Manríquez, J., Godínez, L.A., 2007. Thin Solid Films 515, 3402.
Naseema, S., Khanb, W., Khana, S., Husain, S., Ahmad, A., 2018. J. Magn. Magn. Mater. 447, 155.
Peralta-Hernández, J.M., Manríquez, J., Meas-Vong, Y., Rodríguez, F.J., Chapman, T.W., Maldonado, M.I., Godínez, L.A., 2007. J. Hazard. Mater. 147, 588.
Pletcher, D., 1991. A First Course in Electrode Processes, The Electrochemical Consultancy, Hants, p. 5.
Priyanka, K.P., Sheena, P.A., Sabu, N.A., George, T., Balakrishna, K. M., Varghese, T., 2014. Indian J. Phys. 88, 657.
Raj, K.J.A., Viswanathan, B., 2009. Indian J. Chem. 48A, 1378.
Ren, R., Wen, Z., Cui, S., Hou, Y., Guo, X., Chen, J., 2015. Sci. Rep. 5, 10714.
Salopek, B., Krasić, D., Filipović, S., 1992. Rudarsko-geološko-naftni zbornik 4, 147.
Shen, X., Tian, B., Zhang, J., 2013. Catal. Today 201, 151.
Si, Y., Liu, H., Li, N., Zhong, J., Li, J., Ma, D., 2018. Mater. Lett. 212, 147.
Tran, H.T.T., Kosslick, H., Ibad, M.F., Fischer, C., Bentrup, U., Vuong, T.H., Nguyen, L.Q., Schulz, A., 2017. Appl. Catal. B 200, 647.
Viter, R., Smyntyna, V., Starodub, N., Tereshchenko, A., Kusevitch, A., Doychoa, I., Geveluk, S., Slishik, N., Buk, J., Duchoslav, J., Lubchuk, J., Konup, I., Ubelis, A., Spigulis, J., 2012. Proc. Eng. 47, 338.
Viter, R., Tereshchenko, A., Smyntyna, V., Ogorodniichuk, J., Starodub, N., Yakimova, R., Khranovskyy, V., Ramanavicius, A., 2017. Sens. Actuators, B 252, 95–102.
Wang, Y., Huang, X., Li, H., Guo, L., 2017. Mater. Sci. Eng., C 77, 867.
Yao, M., Zhao, J., Lv, S., Lu, K., 2017. Ceram. Int. 43, 6925.
Yi, Y., Weinberg, G., Prenzel, M., Greiner, M., Heumann, S., Becker, S., Schögl, R., 2017. Catal. Today 295, 32.
Zhou, X., Wu, J., Zhang, J., He, P., Ren, J., Zhang, J., Lu, J., Liang, P., Xu, K., Shui, F., 2017. Mater. Lett. 205, 173.